

Radiation Protection around High-Intensity Laser Interactions with Solid TargetsTaiee Ted Liang^{1*}, Johannes M. Bauer¹, James C. Liu¹, Sayed H. Rokni¹¹SLAC National Accelerator Laboratory, Menlo Park, CA 94025*Corresponding author: tliang6@slac.stanford.edu*Abstract*

Interaction of a high-intensity optical laser with a solid target can generate an ionizing radiation hazard in the form of high-energy ‘hot’ electrons and bremsstrahlung, resulting from hot electrons interacting with the target itself and the surrounding target chamber. Previous studies have characterized the bremsstrahlung dose yields generated by such interactions for lasers in the range of 10^{17} to 10^{22} W cm⁻² using particle-in-cell code EPOCH and Monte Carlo code FLUKA. In this paper, electron measurements based on a depth-dose approach are presented for two laser intensities, which indicate a Maxwellian distribution is more suitable for estimating the hot electrons’ energy distribution. Also, transmission factors of the resulting bremsstrahlung for common shielding materials are calculated with FLUKA, and shielding tenth value layer thicknesses are also derived. In combination with the bremsstrahlung dose yield, the tenth value layers provide radiation protection programs the means to evaluate radiation hazards and design shielding for high-intensity laser facilities.

Introduction

The current count of high-intensity laser facilities worldwide numbers upwards of 69 with 19 based in North America, 32 in Europe, and 18 in Asia (ICUIL; <https://www.icuil.org/activities/laser-labs.html>). Experimenters at these facilities focus multi-terawatt and petawatt optical laser beams to micrometer spot sizes to achieve laser intensities in excess of 10^{17} W cm⁻². One such laser facility is the Matter in Extreme Conditions (MEC) instrument at SLAC National Accelerator Laboratory (Nagler et al. 2015). These high-intensity lasers can be focused onto solid foils to study warm dense matter physics (Fletcher et al. 2015), pressure-driven shock waves in solid materials (Kraus et al. 2016, Wehrenberg et al. 2017), and conditions inside giant planets like Jupiter and Neptune (Davis et al. 2016, Kraus et al. 2017). With gas jets or cells for targets, high-intensity lasers can even be used to produce energetic beams of protons (Gauthier et al. 2016) and electrons and betatron X-rays (Albert et al. 2013). In the coming years, many high-intensity laser facilities worldwide, including the one at MEC, are planning upgrades to achieve even higher laser intensities and pulse repetition rates, which will permit scientists to achieve higher pressure and temperature conditions for their experiments.

These laser facilities present a unique health physics challenge: ionizing radiation generated from optical laser light. The interaction of a high-intensity optical laser with a solid foil target in vacuum creates a plasma on the surface of the target, and subsequent interactions between the laser pulse and the plasma can accelerate plasma electrons to tens and even hundreds of MeV in energy (Tajima and Dawson 1979, Wilks and Kruer 1997). The electrons in this laser-plasma source term are commonly referred to as ‘hot’ electrons and their interactions with both the solid foil and the target chamber wall will generate bremsstrahlung photons (Guo et al. 2001, Chen et

al. 2004). The bremsstrahlung dose generated by a high-intensity optical laser can present an ionizing radiation hazard to personnel in the vicinity.

Over the years, radiation dose measurements from laser facilities such as at the Laboratory for the Use of Intense Lasers (Borne et al. 2002), Rutherford Appleton Laboratory's Vulcan facility (Clarke et al. 2006), Lawrence Livermore National Laboratory's Titan facility (Bauer et al. 2011), and SLAC National Accelerator Laboratory's MEC facility (Liang et al. 2017a) have reported radiation dose levels that require radiation shielding to mitigate direct exposure to personnel at these laser facilities. In addition, the radiation dose scales with laser intensity and is also proportional to the number of laser shots taken on target. From a health physics perspective, understanding the radiation source terms and designing adequate radiation shielding for high-intensity laser facilities such as the aforementioned ones are crucial, especially in light of future upgrades for pre-existing laser facilities and plans for new ones worldwide.

In this paper, the hot electron source term and subsequent bremsstrahlung dose yield from laser interactions with solid targets are reviewed. In addition, an analysis of electron measurements based on a depth-dose approach is presented for two laser intensities. Transmission factors of the resulting bremsstrahlung for common shielding materials are calculated with Monte Carlo code FLUKA (Ferrari et al. 2005, Böhlen et al. 2014), and shielding tenth value layer (TVL) thicknesses are then derived for laser intensities in the range of 10^{17} to 10^{22} W cm⁻². Therefore, health physicists may use the bremsstrahlung dose yield and the calculated TVL thicknesses to design radiation shielding for high-intensity laser facilities.

Hot Electron Source Term

A previous study at SLAC National Accelerator Laboratory (SLAC) characterized the hot electron source term for laser interactions with solid targets for the purpose of radiation protection

(Liang et al. 2017b). The study used the particle-in-cell (PIC) code EPOCH (Arber et al. 2015) to characterize the energy distribution, angular distribution, and laser-to-electron conversion efficiency of hot electrons. In addition, a bremsstrahlung dose yield parameter was defined as the ambient dose equivalent of bremsstrahlung photons from hot electrons and normalized to the laser pulse energy delivered onto the solid target for laser intensities between 10^{17} and 10^{22} W cm⁻². In this way, the bremsstrahlung dose generated from a high-intensity laser-solid experiment could be estimated from laser-optics parameters and the number of laser shots during the experiment.

The key parts of the hot electron source term for the purpose of radiation protection are summarized in this section. The hot electron energy spectrum has been found to fit the Maxwellian distribution given as,

$$f(E) \sim E^{1/2} \exp\left[-\frac{E}{T_h}\right], \quad (1)$$

where E is the electron energy and T_h is the hot electron temperature that characterizes the ‘slope’ of the distribution. Fig. 1 shows an example of the hot electron energy distribution calculated using EPOCH for a laser intensity of 10^{20} W cm⁻², where T_h has a fitted value of 2.1 MeV.

Other studies have used the relativistic Maxwellian distribution in Equation 2 below to approximate the hot electron source term.

$$f(E) \sim E^2 \exp\left[-\frac{E}{T_h}\right]. \quad (2)$$

Both the Maxwellian (Equation 1) and relativistic Maxwellian (Equation 2) have been used to model the hot electron source (Wilks and Kruer 1997, Ledingham et al. 2000, Borne et al 2002). For example, the radiation protection paper by Hayashi et al. (2006) utilized the relativistic Maxwellian distribution for the hot electron source for estimating radiation doses generated by high-power lasers (Hayashi et al. 2006). However, this method using a relativistic Maxwellian has been found to be overly conservative and can overestimate the measured bremsstrahlung dose

generated by hot electrons by up to two orders of magnitude for laser intensities greater than 10^{19} W cm⁻² (Liang et al. 2017a).

For a laser wavelength of 0.8 μm , the hot electron temperature T_h in MeV scales with laser intensity I in W cm⁻² as,

$$T_h = 1.05 \times 10^{-10} I^{0.514}. \quad (3)$$

In Fig. 2, this T_h scaling is compared with results based on PIC code from studies by Wilks (Wilks and Kruer 1997) and Kluge (Kluge et al. 2011).

The angular distribution of the hot electron emission generated from a high-intensity laser was analyzed using EPOCH and was approximated with a simple Gaussian distribution as,

$$f(\theta) \sim \exp\left[-\frac{\theta^2}{2\sigma^2}\right], \quad (4)$$

where θ is the polar angle of the hot electron emission and with a standard deviation σ of 45°. This assumption for the source term results in a more forward-peaked hot electron emission. Other studies (Moore et al. 1995, Yang et al. 2017) have also simply modeled the hot electrons' emission angles as a function of their energy using the relativistic mass factor γ of the hot electron as,

$$\theta = \tan^{-1} \sqrt{\frac{2}{\gamma-1}}. \quad (5)$$

In addition, the ratio of hot electrons emitted in the laser's forward direction versus backward direction (or downstream versus upstream from the laser's target) must also be considered. This ratio was calculated using EPOCH to scale with laser intensity as,

$$r(I) = 2.8 \times 10^{-9} I^{0.46}, \quad (6)$$

where I is the laser intensity in units of W cm⁻². At higher laser intensities, the hot electron emission and the subsequent bremsstrahlung dose generated will be much more forward-peaked. For radiation protection, more radiation shielding would be needed in the laser's forward direction compared to the 90° directions.

The fraction of the laser pulse's energy converted into hot electrons' energy is the laser-to-electron conversion efficiency η . Fig. 3 plots the values of η from EPOCH calculations and indicates the conversion efficiency scales with laser intensity from about 10% at 10^{17} W cm⁻² up to a maximum of 60% starting at 10^{21} W cm⁻².

Electron Depth-Dose Measurements

Electron depth-dose measurements were performed with a simple 'spectrometer' design during two high-intensity laser-solid experiment at SLAC's MEC laser facility (Liang et al. 2017a). One experiment was performed at a laser intensity of 10^{19} W cm⁻² (I_1), which used metal foils of 100- μ m-thick pure Cu (I_1 -Run1) and 15- μ m-thick pure Ni (I_1 -Run2). Another experiment at 7.1×10^{19} W cm⁻² (I_2) was performed parasitically to another experiment. Therefore, there was no control over when the target chamber was opened, when spectrometers (and dosimeters) inside could be replaced, or what target types were used. I_2 -Run3 used a 15- μ m-thick pure Ni foil, and I_2 -Run4 used an assortment of foils: 10 μ m Al, 5 μ m Au, 5 μ m Cu (all pure metal), and 4 μ m CH₃ plastic.

Spectrometers were deployed inside the target vacuum chamber at various angles relative to the laser beam direction and at a distance of 30 cm from the laser's target. They measured dose from both electrons and bremsstrahlung photons inside the target chamber, but the dose deposited in the spectrometer is dominated by the electrons that stream from the laser-solid interaction location without being attenuated by the thin micrometer foils. Fig. 4 shows the layout inside the MEC target chamber from the I_1 experiment at 10^{19} W cm⁻². The approximate locations of the I_1 spectrometers are indicated with a 'star' symbol. Care was taken to ensure the front face of the spectrometers had direct line-of-sight to the target foils at the center of the chamber.

The electron spectrometer's design in Fig. 5 consisted of alternating layers of Landauer nanoDot dosimeters (2-mm-thick) and Plexiglas (3-mm-thick, 1.18 g cm^{-3}). The nanoDot's geometry was simulated in FLUKA as a 0.5-mm-thick aluminum oxide (Al_2O_3 , 3.95 g cm^{-3}) 'wafer' with radius of 2.5 mm that is contained within a plastic polyethylene (C_2H_4 , 0.93 g cm^{-3}) pouch with wall thickness of 0.75 mm (total wall thickness of 1.5 mm). The thickness of the air gaps between the Al_2O_3 and the plastic walls of the nanoDot were considered negligibly thin and not included in FLUKA simulations. The Plexiglas layers will attenuate the incident radiation from high-intensity laser-solid interactions. Fig. 6 plots the results from electron depth-dose measurements taken during the I_1 (Run1 and Run2) and I_2 (Run3 and Run4) experiments for spectrometers deployed at different angles relative to the laser direction. The measured absorbed dose is normalized to the number of laser shots taken on target during each Run (mGy per shot) and is then plotted as a function of depth of attenuating material (g cm^{-2}). The uncertainty in the measured doses is less than 10% and is not plotted in Fig. 6 to avoid visual clutter.

As expected, the (absorbed) dose per shot is higher from I_2 compared to I_1 because a higher laser intensity is both correlated with an increase in the energy of generated hot electrons (Equation 3) and an increase in the laser-to-electron conversion efficiency (Fig. 3). For I_1 the dose per shot measured by the first dosimeter (0 g cm^{-2}) is about 10-15 mGy per shot and decreases by about three orders of magnitude to 0.01-0.03 mGy per shot at the last dosimeter (about 1.8 g cm^{-2}). For I_2 the decrease is two orders of magnitude starting from 20-30 to 0.2-0.3 mGy per shot. This indicates that the energy of the hot electrons for I_1 is lower (and more readily attenuated) than I_2 . The spread of data for all I_1 Runs is within about a factor of 2, which shows the systematic uncertainty of the measured absorbed dose to different target types and detector angles. The factor

of 2 spread in the I_1 dose per shot data for different detector angles also suggests that the angular distribution of hot electron emission is semi-isotropic for I_1 (10^{19} W cm⁻²).

The depth-dose response of the electron spectrometers was benchmarked with FLUKA simulations. PRECISIO was used as the defaults for the simulations. The hot electron source was generated by sampling primary electrons' energies according to a Maxwellian distribution (Equation 1) with FLUKA's custom SOURCE subroutine. The hot electron temperature T_h that characterizes the slope of the energy distribution was calculated from Equation 3 based on the experiments' peak laser intensities. The angular distribution of the electron primaries were sampled according to a Gaussian distribution (Equation 4) with σ of 45° also with SOURCE. Transport and production of electrons and photons were all set at 1 keV threshold. To match experimental conditions in the FLUKA simulation, primary electrons first interacted with a target matching the ones used during the I_1 and I_2 experiments. In addition, the simulated spectrometer was located with the same angle as from the experiment inside a simplified cylindrical model of the experimental chamber: 1 m radius, 1.2 m height, 2.54-cm-thick Al walls.

Additional FLUKA simulations were also performed where the hot electron source term was instead sampled according to a relativistic Maxwellian (Equation 2). For health physics applications, it is necessary to identify the more appropriate energy distribution to model the hot electron source term because this directly affects the magnitude of the estimated radiation hazard and also the design of the radiation shielding needed to mitigate said hazard.

The FLUKA simulations scored the energy (absorbed dose) deposited in the layers of the spectrometer, and depth-dose curves were generated after normalizing the FLUKA results to the same metric as from Fig. 6: dose per shot (mGy per shot) as a function of depth of attenuating material (g cm⁻²). Fig. 7 plots the FLUKA-calculated depth-dose response for the I_1 experiment at

$10^{19} \text{ W cm}^{-2}$, which used 100- μm -thick Cu (Run1) and 15- μm -thick Ni (Run2) as targets. The ‘dashed’ curves indicate the depth-dose response was calculated from a Maxwellian (Max.) distribution for the hot electron source term, while the ‘solid’ curves indicate the response was from a relativistic Maxwellian (rel. Max.) source term. The uncertainty in the FLUKA-calculated dose results is less than 1% for the first dosimeter and increases with each subsequent dosimeter in the spectrometer stack up to about 15% for the last dosimeter. The spread within the data in Fig. 7 (from either a Maxwellian or relativistic Maxwellian source term) is within about a factor of 2, which is similar to the systematic uncertainty observed from the measured data (Fig. 6) for different detector angles and target types. In comparison, the statistical uncertainty in the T_h from Equation 3 used in the FLUKA simulations for either a Maxwellian or relativistic Maxwellian is less than 10% and would not cause the depth-dose response curves to shift more than a factor of 2.

As observed in Fig. 7, the FLUKA-calculated dose per shot for I_1 is higher at increasing depth of attenuating material from primary electrons with a relativistic Maxwellian energy distribution than a Maxwellian because the spectrum is harder (and more penetrating through material), and the average energy is also higher: $3T_h$ vs. $1.5T_h$, respectively. Also because of this, the decrease of the dose per shot from a Maxwellian source term is more rapid (steeper ‘slope’ of the response curve) for the softer energy spectrum. For both electron source terms (Max. and rel. Max.), the response curve for the spectrometer located at $+36^\circ$ is higher than the other angles by at most a factor of 2, which corresponds to the forward-to-backward emission ratio of hot electrons (Equation 6).

Comparing the measured results (Fig. 6) against the FLUKA-calculated results (Fig. 7) for I_1 ($10^{19} \text{ W cm}^{-2}$), the depth-dose response curves generated from a Maxwellian energy distribution

fit the measurement data better than from a relativistic Maxwellian. To further demonstrate this, the measured dose per shot from each data point (and from each Run) was compared versus its corresponding simulated dose per shot. This ‘ratio’ is plotted in Fig. 8 for FLUKA dose per shot from a Maxwellian source term and in Fig. 9 for dose per shot from a relativistic Maxwellian source term. A similar analysis between measured and simulated dose was also performed for the I_2 experiment ($7.1 \times 10^{19} \text{ W cm}^{-2}$), and the results have also been included in Figs. 8 and 9. The ‘line of equality’ indicating where the ratio between measured versus FLUKA-calculated dose is a value of 1 is plotted as a visual guide. Data from both Figs. 8 and 9 were also curve fitted to a power function. Although the fit is not ideal for Fig. 9 (coefficient of determination $R^2 = 0.806$), the fitted curves $f(x)$ demonstrate visually that the measured data is better predicted with calculations using a Maxwellian source term as seen in in Fig. 8 ($R^2 = 0.936$). Also the ‘slope’ of the fitted power functions has a value of 1.09 for a Maxwellian source term and 0.686 for a relativistic Maxwellian source. Comparing these values against the line of equality (slope of 1), this further supports that a Maxwellian source term is more appropriate for predicting the measured data.

Comparison between Figs. 8 and 9 showed that measured data has a more 1:1 ratio with the simulated results from FLUKA and better predicted using a Maxwellian source term (Fig. 8). This comparison between source terms can be further examined by calculating the mean squared errors (MSE) between the measured data and the simulated results for the two source terms, which is given in Equation 7 as,

$$MSE = \frac{1}{n} \sum_{i=1}^n (M_i - S_i)^2. \quad (7)$$

This method provides a quantitative index for evaluating of the quality of an estimator (the type of source term in this case). Note that it is necessary to take the logarithm of the data and results because their values span a range of 4 orders of magnitude. The MSE between all measured data

and simulated results using a Maxwellian source term (Fig. 8) is 0.183 and using a relativistic Maxwellian source term (Fig. 9) is 0.428. The value of the MSE is smaller for a Maxwellian source, which again supports the use of a Maxwellian distribution to model the hot electron source term and to predict the measured data.

The depth-dose response curves calculated from a Maxwellian source term describe the I_1 and I_2 experiments' measurement data better than the curves calculated from a relativistic Maxwellian source term. From a health physics perspective, it is an improvement and a more accurate representation to model the energies of the hot electron source as a Maxwellian distribution. Otherwise, both estimation of secondary bremsstrahlung dose generated from hot electrons and design of shielding with a relativistic Maxwellian source term would be overly conservative.

Bremsstrahlung Dose Yield

FLUKA can be utilized to calculate the bremsstrahlung dose yield generated from the hot electron source (primary electrons) described previously using FLUKA's custom SOURCE subroutine. The energies of primary electrons were sampled according to a Maxwellian distribution (Equation 1) with exponential slope described by T_h (Equation 3). The angular distribution of primary electrons were sampled according to a Gaussian distribution (Equation 4) with σ of 45° and forward-to-backward emission ratio (Equation 6). The resulting bremsstrahlung dose calculated by FLUKA can be normalized to the laser-to-electron conversion efficiency (Fig. 3). Fig. 10 shows the estimated bremsstrahlung dose yield at 1 meter distance (Liang et al. 2017b) from a high-intensity laser interaction with a solid target for laser intensities between 10^{17} and 10^{22} W cm⁻². The dose yield curves in Fig. 10 already account for attenuation by a simple cylindrical target chamber with uniform 2.54-cm-thick aluminum walls. The dose yield (mSv J⁻¹) parameter

is the ambient dose equivalent (mSv) of bremsstrahlung photons generated from hot electrons and normalized to the laser pulse energy on target (J).

In reality, target vacuum chambers for high-intensity laser experiments often have a complex geometry. Fig. 11 visualizes with SimpleGeo (Theis et al. 2006) the full geometry of MEC's target vacuum chamber, which has a chamber radius of about 1 meter and wall thicknesses of about 2.54-cm-thick aluminum. A large number of glass view ports around the chamber give experimenters access to the vacuum chamber with their instruments.

The hot electron source term can also be paired with a full target chamber geometry in FLUKA to simulate the bremsstrahlung dose generated from individual high-intensity laser experiments, especially if laser-optics and laser target parameters are known. For example, the I₁ experiment at MEC achieved a peak laser intensity of 10^{19} W cm⁻² with a pulse energy of 0.7 J and a pulse length of 50 fs. The laser system operated at a 1 Hz repetition rate and delivered high-intensity laser shots onto 100- μ m-thick Cu foils. The associated source term (primary electrons) was modeled using a Maxwellian energy distribution with a T_h of 0.61 MeV, a Gaussian angular distribution with σ of 45°, a forward-to-backward emission ratio of 1.3, and a laser-to-electron conversion efficiency of 0.51. Fig. 12 plots the bremsstrahlung dose generated per laser shot delivered onto the target foil (mSv per shot) as calculated with FLUKA using the hot electron source term described above. Either the dose yield curves in Fig. 10 or the direct calculation of bremsstrahlung dose with FLUKA using an experiments' parameters and geometries may be used to estimate the dose to personnel from high-intensity laser-solid experiments.

Tenth Value Layers for Bremsstrahlung Photons

High-intensity laser-solid experiments need radiation shielding to mitigate the bremsstrahlung dose hazard generated by the hot electrons. A systematic study with FLUKA used

the hot electron source term modeled with a Maxwellian energy distribution and with T_h derived from laser intensity to calculate transmission factors of several common shielding materials. Transport and production of electrons and photons were all set at 1 keV threshold. The tenth value layer (TVL) thicknesses can then be derived from the transmission curves. In this study, TVL is the thickness of the material needed to reduce the ambient dose equivalent of the incident radiation (bremsstrahlung from hot electrons) by a factor of 10. Previous shielding studies for high-intensity laser facilities have focused primarily on glass, concrete, and lead (Qiu et al. 2006, Yang et al. 2017). While those materials are also included, this study contains TVL thicknesses for other materials not available elsewhere as a function of laser intensity from 10^{17} to 10^{22} W cm⁻²: Pyrex glass* (2.23 g cm⁻³), Portland concrete† (2.3 g cm⁻³), aluminum (2.7 g cm⁻³), iron (7.87 g cm⁻³), lead (11.34 g cm⁻³), and tungsten (19.25 g cm⁻³).

This variety of shielding materials provides health physicists flexibility when designing radiation shielding for high-intensity laser facilities. For example, as many of these facilities receive upgrades to their laser power and intensity, the generated ionizing radiation hazard will also increase (Fig. 10). For pre-existing facilities, it may be impractical both financially and time-wise to demolish and rebuild the facility housing when the wall shielding is no longer sufficient to mitigate the increased hazard. Instead, radiation protection programs may choose to deploy local shielding inside the target vacuum chamber and in close proximity to the laser-solid interaction. When space is limited, lead (Pb) is a commonly chosen shielding material, but it comes with other hazards: chemical toxicity, potential for activation by high-energy bremsstrahlung, and out-gassing that may compromise the vacuum's integrity. Therefore, a discerning health physicist may choose tungsten (W) or steel (Fe) for local shielding instead. Earlier, Fig. 4 showed the layout inside of the target chamber at MEC for the I₁ experiment with laser intensity at 10^{19} W cm⁻².

During this experiment, stainless steel plates amounting to a thickness of 12 cm were used as local shielding in the 0° and 180° directions relative to the laser direction to mitigate the bremsstrahlung dose to personnel outside the facility.

Shielding calculations with FLUKA utilized a spherical geometry. For a chosen laser intensity, primary electrons with energies sampled according to a Maxwellian distribution (Equation 1) and with temperature T_h (Equation 3) were emitted isotropically from the center of a Cu sphere. The Cu sphere ‘target’ served as the electron-to-bremsstrahlung converter, and its radius was optimized to give the highest bremsstrahlung yield from hot electrons. For example, the optimum radius of the Cu sphere target was 2.5 mm at 10^{20} W cm⁻². A spherical shell of the shielding material of interest was located at 10 meters (outer radius) from the source point to attenuate the generated bremsstrahlung photons. The ambient dose equivalent was scored at the same radial distance outside the shield without and with shielding to generate transmission factors for varying shielding thicknesses.

Fig. 13 plots the transmission factors for Portland concrete (CC) as a function of shielding material thickness for selected laser intensities between 10^{17} and 10^{22} W cm⁻². The uncertainties of the estimated transmission factors were at most less than 3%. Increasing thicknesses for the shielding were selected for increasing laser intensities because the average energy of the hot electrons (and resulting bremsstrahlung) increases as well. A material’s photon mass attenuation coefficient decreases with increasing photon energy, which means more material thickness is needed to achieve the same attenuation factor for higher energy bremsstrahlung by the same factor.

Also in Fig. 13 at higher laser intensities where the energy of hot electrons is also higher, a buildup factor is observed where the transmission curve experiences a change in slope or a ‘kink’ for 3×10^{21} and 10^{22} W cm⁻² (at 14 and 16 cm, respectively). At these intensities, the hot electron

source has energies in the 10's of MeV and greater. The TVLs of concrete can be derived from the transmission curves for concrete for the selected laser intensities by taking the concrete thicknesses corresponding to a bremsstrahlung transmission factor of 0.1 and 0.01 (Fig. 13). The transmission of bremsstrahlung dose decreases as more shielding material is added to attenuate the incident bremsstrahlung. TVL_1 corresponds to the material thickness required to reduce the incident bremsstrahlung dose by a factor of 10. TVL_2 is the thickness needed to reduce the dose by an additional factor of 10. As observed in Fig. 13, TVL_2 is also the equilibrium tenth value layer (TVL_e), which is the thickness for each subsequent TVL after TVL_1 where the directional and spectral distributions of the radiation field in the material are practically independent of thickness.

Fig. 14 provides the transmission curves for Pb, which is a higher Z and higher density material than Portland concrete, and the thickness of lead required to achieve a transmission factor of 0.1 and 0.01 is much less than for concrete at any selected laser intensity. At lower laser intensities especially around $3 \times 10^{18} \text{ W cm}^{-2}$ and below, the transmission factor curves for Pb has a dramatic first drop due to strong filtering of lower energies by Pb.

The values of Portland concrete TVL_1 and TVL_e for bremsstrahlung photons generated by a hot electron source are plotted in Fig. 15. TVL_1 is significantly greater than TVL_e at laser intensities greater than $3 \times 10^{21} \text{ W cm}^{-2}$ due to buildup. At these higher laser intensities, the Maxwellian energy distribution of the hot electron source is characterized by a T_h of 21 MeV (Equation 3) and has a high average energy of about 32 MeV. The subsequently generated bremsstrahlung is also high energy and causes buildup in the shielding material. Therefore, additional concrete shielding is initially required for TVL_1 to reduce the incident bremsstrahlung dose by a factor of 10.

TVL₁ and TVL_e for lead and tungsten are similarly plotted in Figs. 16 and 17, respectively. The effect of buildup is more pronounced for Pb and W (higher Z material) than for concrete, and TVL₁ is again greater than TVL_e at laser intensities greater than 10²⁰ W cm⁻². At intensities below the TVL₁ and TVL_e crossover, TVL₁ is lower than TVL_e due to strong filtering of the incident bremsstrahlung's lower energy components by Pb and W. This effect between TVL₁ and TVL_e was also observed for Pb TVLs by Yang et al. (2017). TVL_e for Pb and W begin to plateau starting at about 10²⁰ W cm⁻², which corresponds to the high-energy limit or 'Compton minimum' of the high energy photons.

Figs. 18 and 19 summarize the values of TVL₁ and TVL_e for Pyrex glass, Portland concrete, Al, Fe, Pb, and W as a function of laser intensity between 10¹⁷ and 10²² W cm⁻². As expected, materials with higher Z and density such as Pb and W are most effective for shielding photons and require less material to attenuate the incident bremsstrahlung dose compared with the other materials at a given laser intensity. Glass, concrete, and Al have very similar values of TVL due to having similar densities and also similar effective Z. The overall bremsstrahlung energy (and hot electron temperature) increases as the laser intensity increases (Fig. 2), and the opposite is also true. For laser intensities below 10¹⁸ W cm⁻² where the hot electron temperature is in the tens of keV, there is a rapid drop in the TVL because photon mass attenuation coefficients are high due to the effect of high photoelectric cross sections at those energies.

When designing radiation shielding using Figs. 18 and 19, the thickness of TVL₁ can be larger than TVL_e at high laser intensities due to buildup, so radiation shielding for a high-intensity laser's hot electron source that requires multiple TVLs should use the TVL₁ thickness for the first TVL and then TVL_e thickness for each subsequent TVL.

Conclusion

In this paper, the hot electron source term and resulting bremsstrahlung dose yield for high-intensity laser interactions with solid targets were summarized. Analysis of electron depth-dose measurements from two experiments at 10^{19} (I_1) and 7.1×10^{19} W cm^{-2} (I_2) demonstrated that a Maxwellian energy distribution is a more appropriate model for the hot electron source term than a relativistic Maxwellian. FLUKA simulations with a hot electron source term with energy sampled according to a Maxwellian distribution were systematically conducted, and the transmission factors of common shielding materials (Pyrex glass, Portland concrete, Al, Fe, Pb, and W) were obtained for the ambient dose equivalent of bremsstrahlung photons generated by hot electrons as a function of laser intensity between 10^{17} and 10^{22} W cm^{-2} . The tenth value layers TVL_1 and TVL_e were derived from these transmission curves for each of the materials. In combination with the hot electron source term and bremsstrahlung dose yield estimations, health physicists will be able to utilize these TVL thicknesses to design radiation shielding for mitigation of bremsstrahlung dose at high-intensity laser facilities.

Acknowledgements

The authors wish to thank R. Clarke of Rutherford Appleton Laboratory for lending the electron spectrometers used in the depth-dose measurements.

This material is based upon work supported by the U.S. Department of Energy, Office of Science, Office of Basic Energy Sciences, under Contract No. DE-AC02-76SF00515.

References

- Albert F, Pollock BB, Shaw JL, Marsh KA, Ralph JE, Chen YH, Alessi D, Pak A, Clayton CE, Glenzer SH, Joshi C. Angular Dependence of Betatron X-Ray Spectra from a Laser-Wakefield Accelerator. *Physical Review Letters* 111:235004; 2013.
DOI:10.1103/PhysRevLett.111.235004
- Arber TD, Bennett K, Brady CS, Lawrence-Douglas A, Ramsay MG, Sircombe NJ, Gillies P, Evans RG, Schmitz H, Bell AR. Contemporary particle-in-cell approach to laser-plasma modelling. *Plasma Physics and Controlled Fusion* 57:113001; 2015.
DOI:10.1088/0741-3335/57/11/113001
- Bauer J, Liu JC, Prinz AA, Tran H, Xia Z. High Intensity Laser Induced Radiation Measurements at LLNL. *SLAC Radiation Physics Note RP-11-11:1-16*; 2011.
- Böhlen TT, Cerutti F, Chin MPW, Fassò A, Ferrari A, Ortega PG, Mairani A, Sala PR, Smirnov G, Vlachoudis V. The FLUKA Code: Developments and Challenges for High Energy and Medical Applications. *Nuclear Data Sheets* 120:211-214; 2014.
DOI:10.1016/j.nds.2014.07.049
- Borne F, Delacroix D, Gelé JM, Massé D, Amiranoff F. Radiation Protection for an Ultra-high Intensity Laser. *Radiation Protection Dosimetry* 102:61-70; 2002.
DOI:10.1093/oxfordjournals.rpd.a006074
- Chen LM, Forget P, Fourmaux S, Kieffer JC, Krol A, Chamberlain CC, Hou BX, Nees J, Mourou G. Study of hard x-ray emission from intense femtosecond Ti:sapphire laser-solid target interactions. *Physics of Plasmas* 11:4439; 2004. DOI:10.1063/1.1781625
- Clarke RJ, Neely D, Edwards RD, Wright PNM, Ledingham KWD, Heathcote R, McKenna P, Danson CN, Brummitt PA, Collier JL, Hatton PE, Hawkes SJ, Hernandez-

- Gomez C, Holligan P, Hutchinson MHR, Kidd AK, Lester WJ, Neville DR, Norreys PA, Pepler DA, Winstone TB, Wyatt RWW, Wyborn BE. Radiological characterisation of photon radiation from ultra-high-intensity laser–plasma and nuclear interactions. *Journal of Radiological Protection* 26:277-286; 2006. DOI:10.1088/0952-4746/26/3/002
- Davis P, Döppner T, Rygg JR, Fortmann C, Divol L, Pak A, Fletcher L, Becker A, Holst B, Sperling P, Redmer R, Desjarlais MP, Celliers P, Collins GW, Landen OL, Falcone RW, Glenzer SH. X-ray scattering measurements of dissociation-induced metallization of dynamically compressed deuterium. *Nature Communications* 7:11189; 2016. DOI:10.1038/ncomms11189
 - Ferrari A, Sala PR, Fassò A, Ranft J. FLUKA: a multi-particle transport code. CERN-2005-10, INFN/TC_05, SLAC-R-773; 2005.
 - Fletcher LB, Lee HJ, Döppner T, Galtier E, Nagler B, Heimann P, Fortmann C, LePape S, Ma T, Millot M, Pak A, Turnbull D, Chapman DA, Gericke DO, Vorberger J, White T, Gregori G, Wei M, Barbrel B, Falcone RW, Kao CC, Nuhn H, Welch J, Zastra U, Neumayer P, Hastings JB, Glenzer SH. Ultrabright X-ray laser scattering for dynamic warm dense matter physics. *Nature Photonics* 9:274-279; 2015. DOI:10.1038/nphoton.2015.41
 - Gauthier M, Kim JB, Curry CB, Aurand B, Gamboa EJ, Göde S, Goyon C, Hazi A, Kerr S, Pak A, Propp A, Ramakrishna B, Ruby J, Willi O, Williams GJ, Rödel C, Glenzer SH. High-intensity laser-accelerated ion beam produced from cryogenic micro-jet target. *Review of Scientific Instruments* 87:11D827; 2016. DOI:10.1063/1.4961270
 - Guo T, Spielmann Ch, Walker BC, Barty CPJ. Generation of hard x rays by ultrafast terawatt lasers. *Review of Scientific Instruments* 72:41; 2001. DOI:10.1063/1.1327309

- Hayashi Y, Fukumi A, Matsukado K, Mori M, Kotaki H, Kando M, Chen LM, Daito I, Kondo S, Kanazawa S, Yamazaki A, Ogura K, Nishiuchi M, Kado M, Sagisaka A, Nakamura S, Li Z, Orimo S, Homma T, Daido H. Estimation of photon dose generated by a short pulse high power laser. *Radiation Protection Dosimetry* 121:99-107; 2006. DOI:10.1093/rpd/nci383
- International Committee on Ultra-High Intensity Lasers (ICUIL). Intense Laser Labs World Wide [online]. Available at: <https://www.icuil.org/activities/laser-labs.html>. Accessed 8 November 2017.
- Kluge T, Cowan T, Debus A, Schramm U, Zeil K, Bussmann M. Electron Temperature Scaling in Laser Interaction with Solids. *Physical Review Letters* 107:205003; 2011. DOI:10.1103/PhysRevLett.107.205003
- Kraus D, Ravasio A, Gauthier M, Gericke DO, Vorberger J, Frydrych S, Helfrich J, Fletcher LB, Schaumann G, Nagler B, Barbrel B, Bachmann B, Gamboa EJ, Göde S, Granados E, Gregori G, Lee HJ, Neumayer P, Schumaker W, Döppner T, Falcone RW, Glenzer SH, Roth M. Nanosecond formation of diamond and lonsdaleite by shock compression of graphite. *Nature Communications* 7:10970; 2016. DOI:10.1038/ncomms10970
- Kraus D, Vorberger J, Pak A, Hartley NJ, Fletcher LB, Frydrych S, Galtier E, Gamboa EJ, Gericke DO, Glenzer SH, Granados E, MacDonald MJ, MacKinnon AJ, McBride EE, Nam I, Neumayer P, Roth M, Saunders AM, Schuster AK, Sun P, van Driel T, Döppner T, Falcone RW. Formation of diamonds in laser-compressed hydrocarbons at planetary interior conditions. *Nature Astronomy* 1:606-611; 2017. DOI:10.1038/s41550-017-0219-

- Ledingham KWD, Spencer I, McCanny T, Singhal RP, Santala MIK, Clark E, Watts I, Beg FN, Zepf M, Krushelnick K, Tatarakis M, Dangor AE, Norreys PA, Allott R, Neely D, Clark RJ, Machacek AC, Wark JS, Cresswell AJ, Sanderson DCW, Magill J. Photonuclear Physics when a Multiterawatt Laser Pulse Interacts with Solid Targets. *Physical Review Letters* 84:899; 2000. DOI:10.1103/PhysRevLett.84.899
- Liang T, Bauer J, Cimeno M, Ferrari A, Galtier E, Granados E, Lee HJ, Liu J, Nagler B, Prinz A, Rokni S, Tran H, Woods M. Radiation Dose Measurements for High-Intensity Laser Interactions with Solid Targets at SLAC. *Radiation Protection Dosimetry* 172:346-355; 2017a. DOI: 10.1093/rpd/ncv505
- Liang T, Bauer JM, Liu JC, Rokni SH. Bremsstrahlung Dose Yield for High-Intensity Short-Pulse Laser-Solid Experiments. *Radiation Protection Dosimetry* 175:304-312; 2017b. DOI:10.1093/rpd/ncw325
- Moore CI, Knauer JP, Meyerhofer DD. Observation of the Transition from Thomson to Compton Scattering in Multiphoton Interactions with Low-Energy Electrons. *Physical Review Letters* 74:2439-2442; 1995. DOI:10.1103/PhysRevLett.74.2439
- Nagler B, Arnold B, Bouchard G, Boyce RF, Boyce RM, Callen A, Campell M, Curiel R, Galtier E, Garofoli J, Granados E, Hastings J, Hays G, Heimann P, Lee RW, Milathianaki D, Plummer L, Schropp A, Wallace A, Welch M, White W, Xing Z, Yin J, Young J, Zastrau U, Lee HJ. The Matter in Extreme Conditions instrument at the Linac Coherent Light Source. *J Synchrotron Rad* 22:520-525; 2015. DOI:10.1107/S16005775150048
- Qiu R, Zhang H, Yang B, Liu JC, Rokni SH, Woods MB, Li JL. Dose estimation and shielding calculation for X-ray hazard at high intensity laser facilities. *Chinese Physics C* 38:129001; 2014. DOI:10.1088/1674-1137/38/12/129001

- Tajima T and Dawson JM. Laser electron accelerator. *Physical Review Letters* 43:267; 1979. DOI:10.1103/PhysRevLett.43.267
- Theis C, Buchegger KH, Brugger M, Forkel-Wirth D, Roesler S, Vincke H. Interactive three dimensional visualization and creation of geometries for Monte Carlo calculations. *Nuclear Instruments and Methods in Physics Research A* 562:827-829; 2006. DOI:10.1016/j.nima.2006.02.125
- Wehrenberg CE, McGonegle D, Bolme C, Higginbotham A, Lazicki A, Lee HJ, Nagler B, Park HS, Remington BA, Rudd RE, Sliwa M, Suggit M, Swift D, Tavella F, Zepeda-Ruiz L, Wark JS. In situ X-ray diffraction measurement of shock-wave-driven twinning and lattice dynamics. *Nature* 550:496-499; 2017. DOI:10.1038/nature24061
- Wilks SC and Kruer WL. Absorption of ultrashort, ultra-intense laser light by solids and overdense plasmas. *IEEE Journal of Quantum Electronics* 33:1954-1968; 1997. DOI:10.1109/3.641310
- Yang B, Qiu R, Li J, Lu W, Wu Z, Li C. Photon dose estimation from ultraintense laser-solid interactions and shielding calculation with Monte Carlo simulation. *Radiation Physics and Chemistry* 131:13-21; 2017. DOI: 10.1016/j.radphyschem.2016.10.010

List of Footnotes

- * 54% O, 37.7% Si, 4% Be, 2.8% Na, 1.2% Al, 0.3% K
- † 52.9% O, 33.7% Si, 4.4% Ca, 3.4% Al, 1.6% Na, 1.4% Fe, 1.3% K, 1% H, 0.2% Mg,
0.1% C

List of Figure Captions

- Fig. 1. Energy distribution of hot electrons calculated from an EPOCH simulation for $10^{20} \text{ W cm}^{-2}$. A Maxwellian fit gives $T_h = 2.1 \text{ MeV}$.
- Fig. 2. Hot electron temperature as a function of laser intensity calculated from EPOCH simulations (Liang et al. 2017b).
- Fig. 3. Laser-to-electron conversion efficiency as a function of laser intensity calculated from EPOCH simulations (Liang et al. 2017b).
- Fig. 4. Layout inside MEC's target chamber for the I₁ laser-solid experiment at $10^{19} \text{ W cm}^{-2}$. The locations of spectrometers deployed inside are indicated with a 'star' symbol. The high-intensity optical laser enters the chamber from the left and interacts with solid metal foils at the center of the chamber.
- Fig. 5. Electron depth-dose spectrometer consisted of alternating layers of Plexiglas and Landauer nanoDot dosimeters. Electrons enter the spectrometer from left-to-right, are attenuated by the Plexiglas, and deposit dose in the dosimeters.
- Fig. 6. Absorbed dose per laser shot (mGy per shot) measured during I₁ (Run1 and Run2) and I₂ (Run3 and Run4) experiments at MEC and plotted as a function of depth of attenuating material (g cm^{-2}).
- Fig. 7. Absorbed dose per laser shot (mGy per shot) calculated from FLUKA simulations for I₁ (Run1 and Run2) experiment using target types and detector angles from the I₁ experiment. The 'dashed' curves indicate results from a Maxwellian (Max.) distribution for the hot electron source term, while the 'solid' curves indicate results from a relativistic Maxwellian (rel. Max.) source term

- Fig. 8. Comparison of measured dose per shot from I₁ and I₂ experiments versus FLUKA-simulated dose per shot calculated with a Maxwellian (Max.) hot electron source term.
- Fig. 9. Comparison of measured dose per shot from I₁ and I₂ experiments versus FLUKA-simulated dose per shot calculated with a relativistic Maxwellian (rel. Max.) hot electron source term.
- Fig. 10. Estimation of bremsstrahlung dose yield outside a simple 2.54-cm-thick Al target vacuum chamber at 1 meter distance from laser-solid interaction as a function of laser intensity from EPOCH and FLUKA calculations (Liang et al. 2017b).
- Fig. 11. Target vacuum chamber located at SLAC's MEC laser facility, which has a radius of 1 meter and approximate Al wall thickness of 2.54 cm.
- Fig. 12. Bremsstrahlung photon dose per laser shot (mSv per shot) at the target plane calculated with FLUKA for the I₁ (10^{19} W cm⁻²) experiment at MEC. In this simulation, the primary electrons interacted with a 100- μ m-thick Cu foil located at the center of the target chamber.
- Fig. 13. Concrete transmission factors as a function of concrete thickness for bremsstrahlung photons generated from a hot electron source and for selected laser intensities (W cm⁻²).
- Fig. 14. Lead transmission factors as a function of lead thickness for bremsstrahlung photons generated from a hot electron source and for selected laser intensities (W cm⁻²).
- Fig. 15. TVL₁ and TVL_e of Portland concrete (CC) as a function of laser intensity for bremsstrahlung photons generated from a hot electron source.
- Fig. 16. TVL₁ and TVL_e of lead (Pb) as a function of laser intensity for bremsstrahlung photons generated from a hot electron source.

- Fig. 17. TVL_1 and TVL_e of tungsten (W) as a function of laser intensity for bremsstrahlung photons generated from a hot electron source.
- Fig. 18. TVL_1 of Pyrex glass, Portland concrete, Al, Fe, Pb, and W as a function of laser intensity for bremsstrahlung photons generated from a hot electron source.
- Fig. 19. TVL_e of Pyrex glass, Portland concrete, Al, Fe, Pb, and W as a function of laser intensity for bremsstrahlung photons generated from a hot electron source.

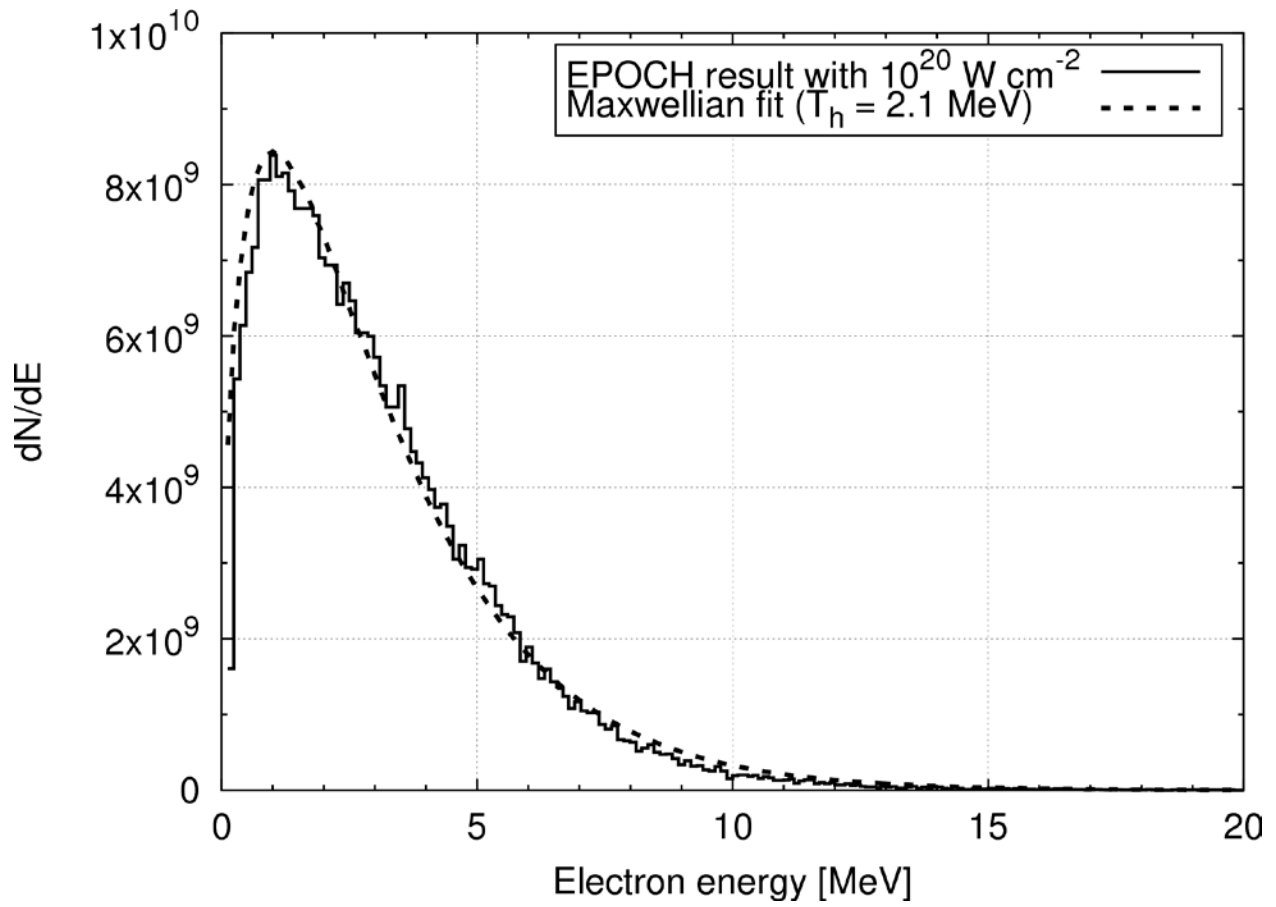


Fig. 1.

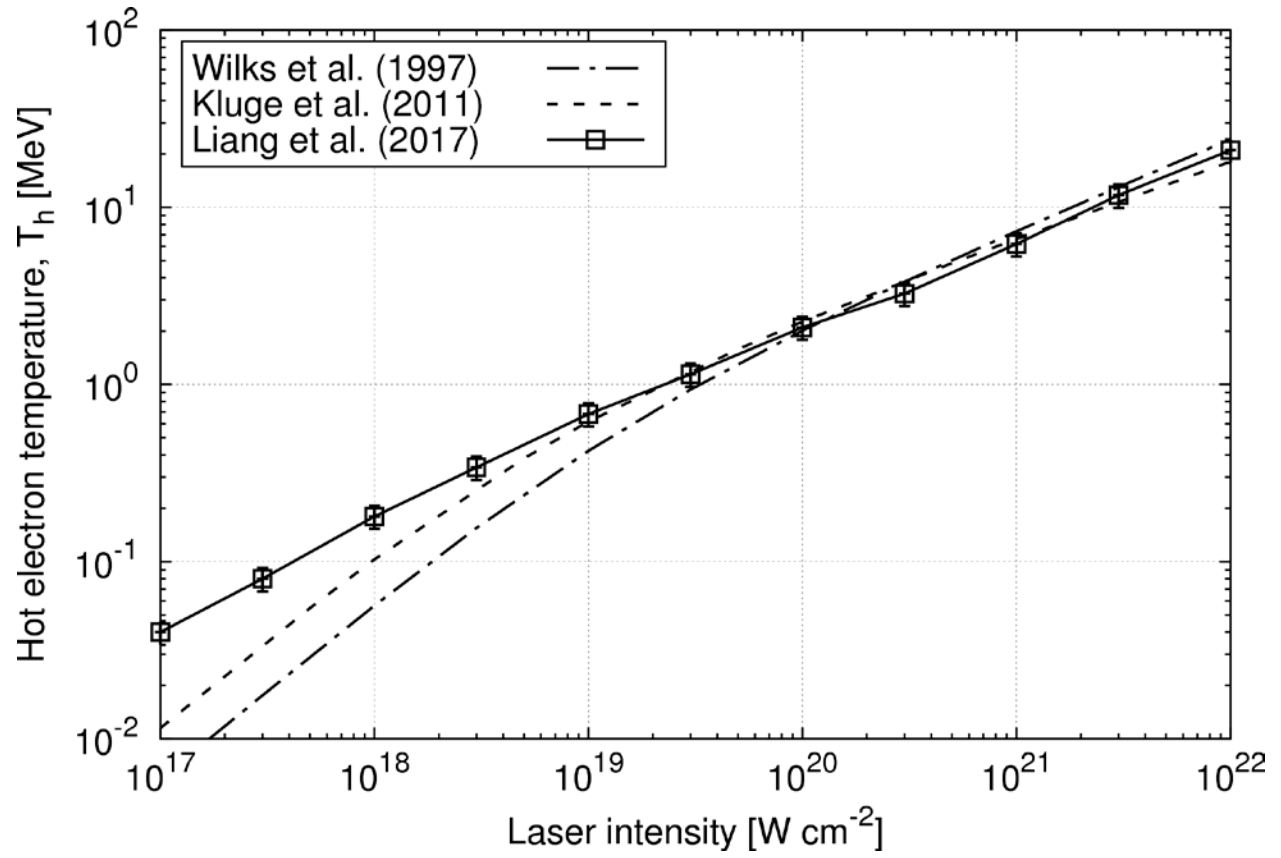


Fig. 2.

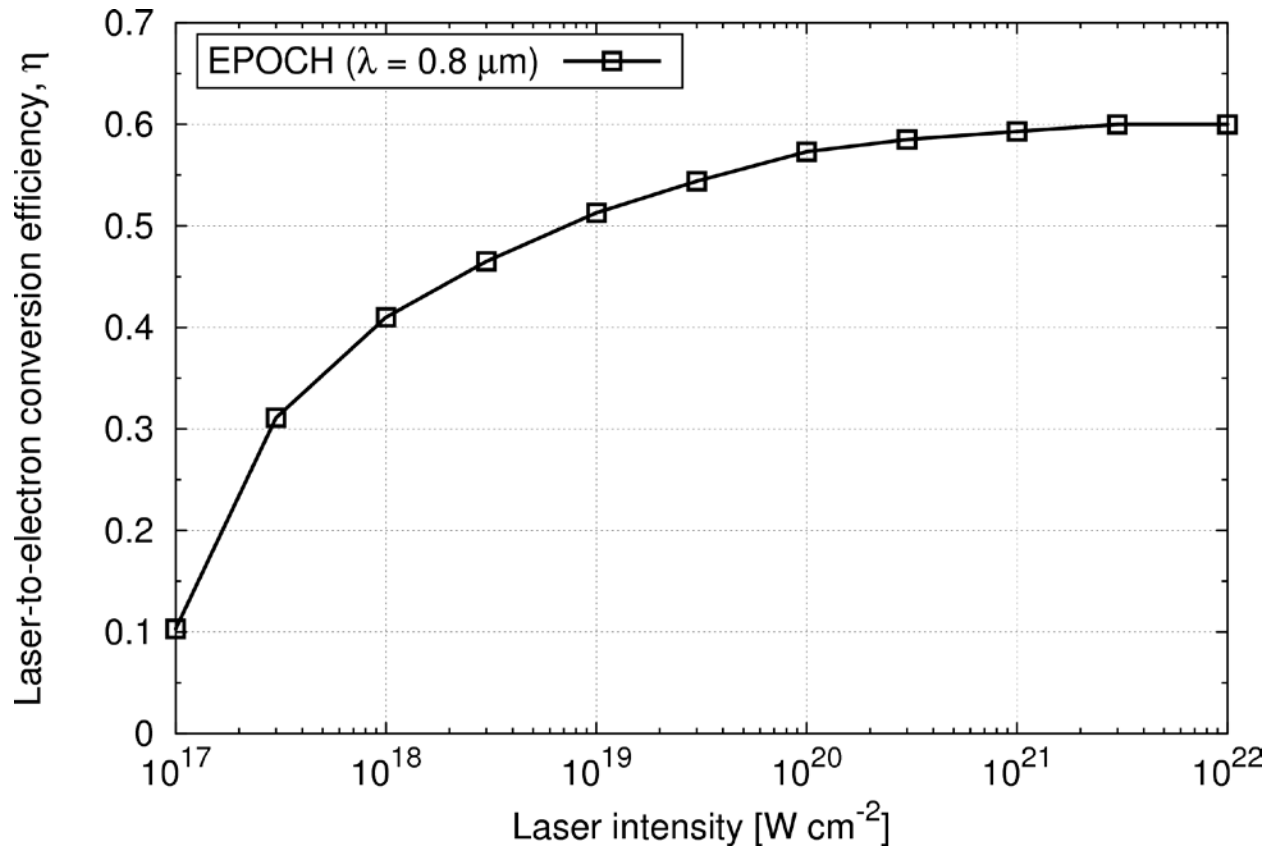


Fig. 3.

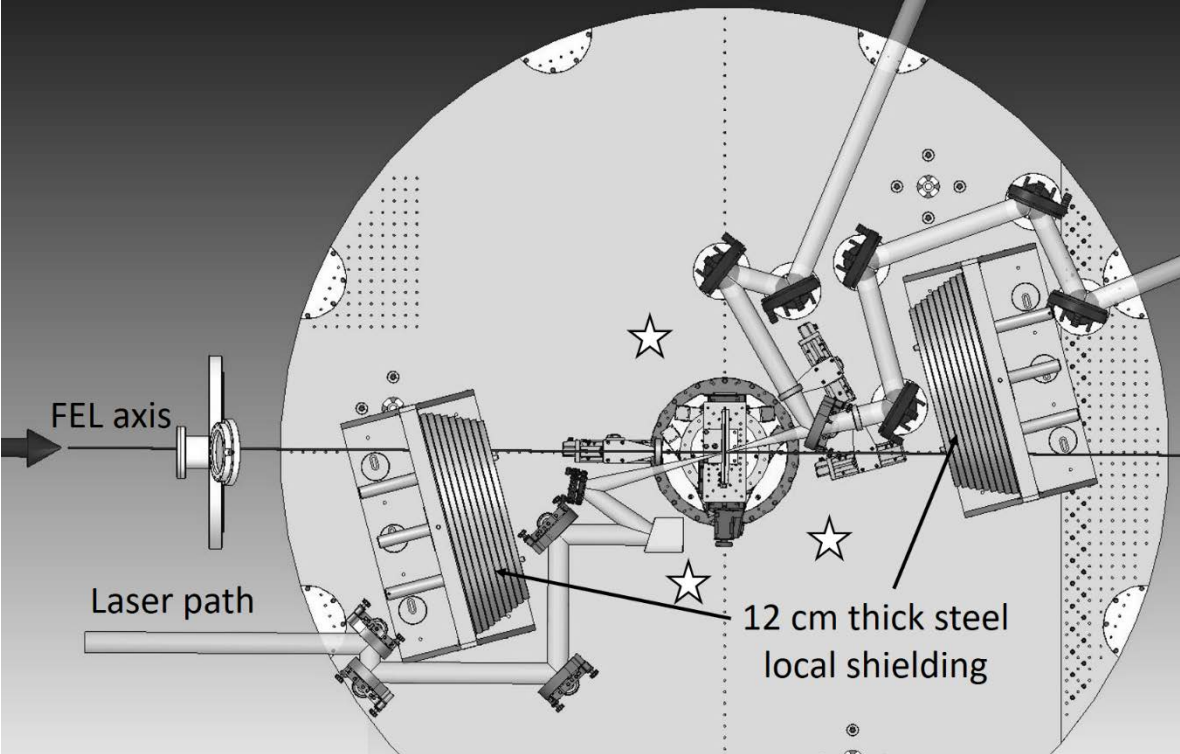


Fig. 4.

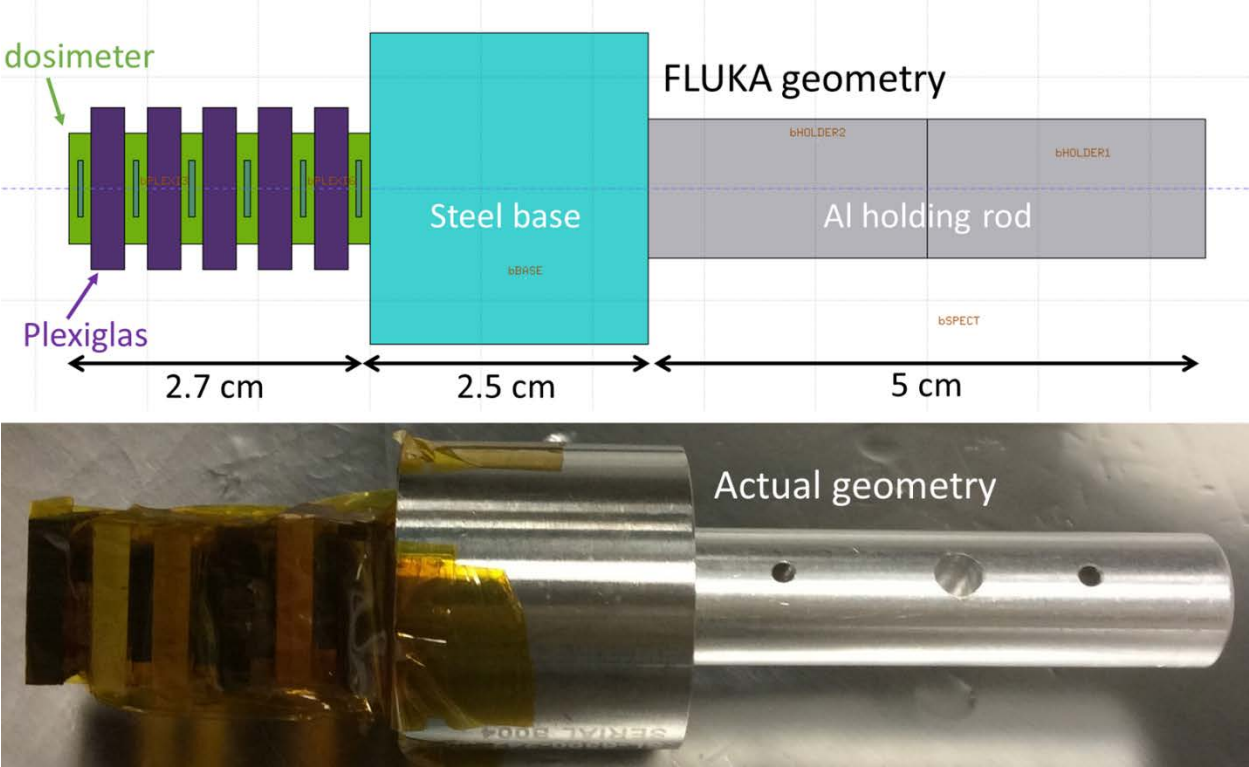


Fig. 5.

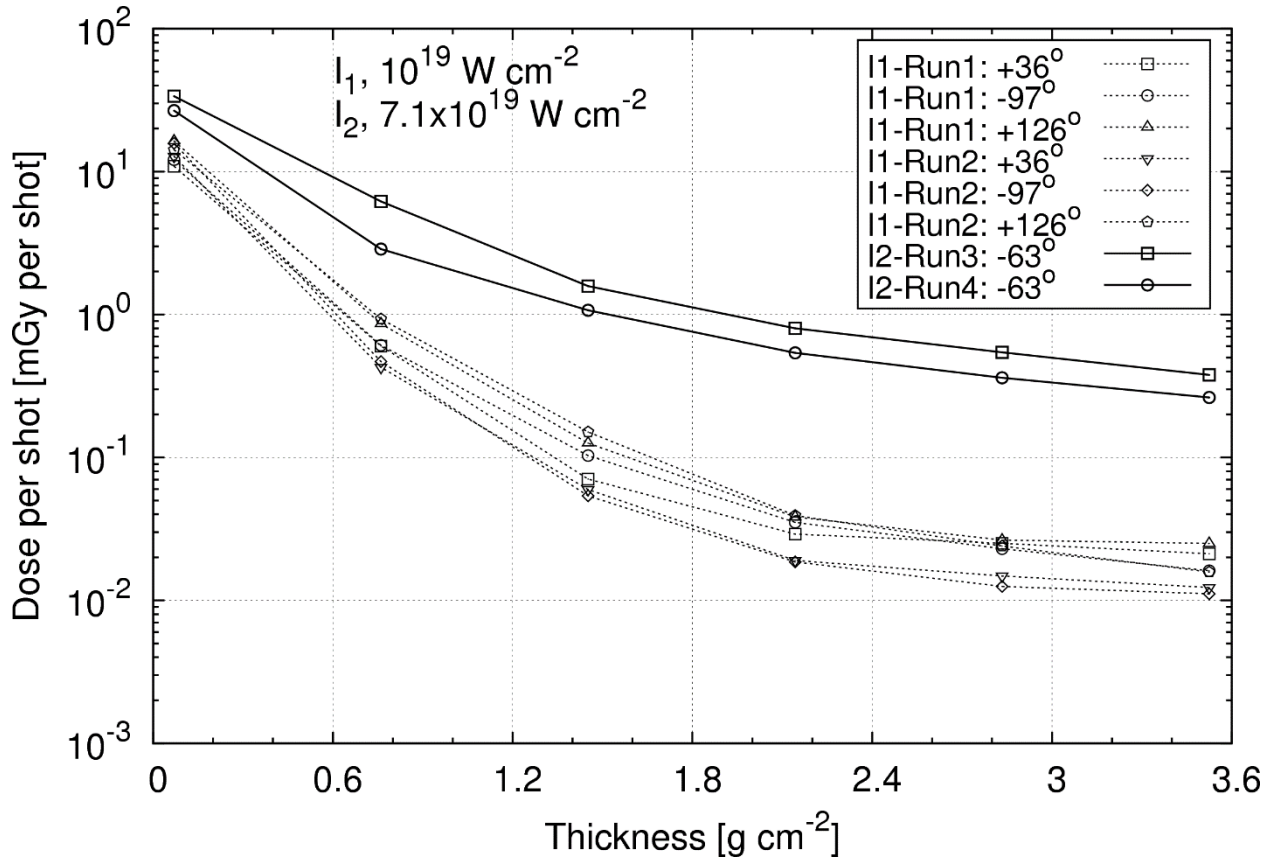


Fig. 6.

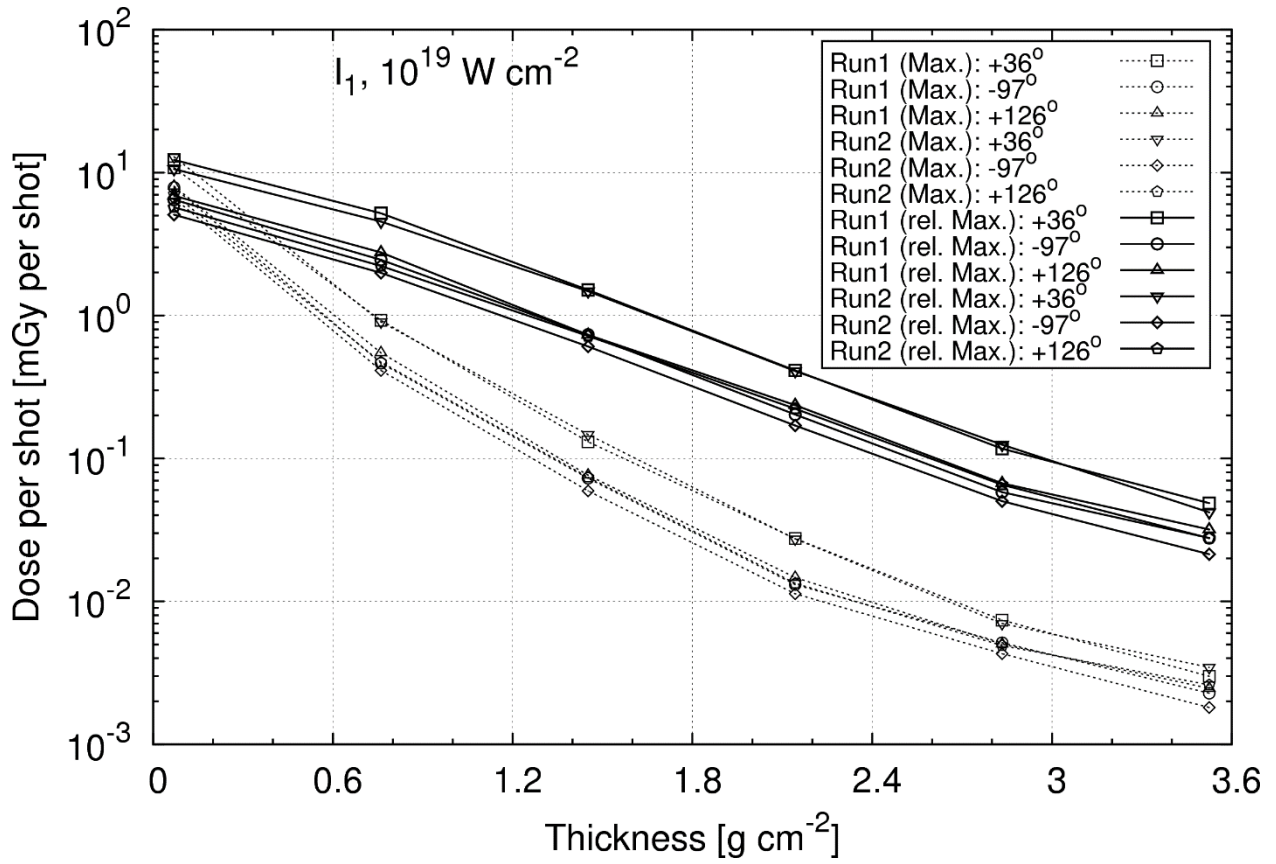


Fig. 7.

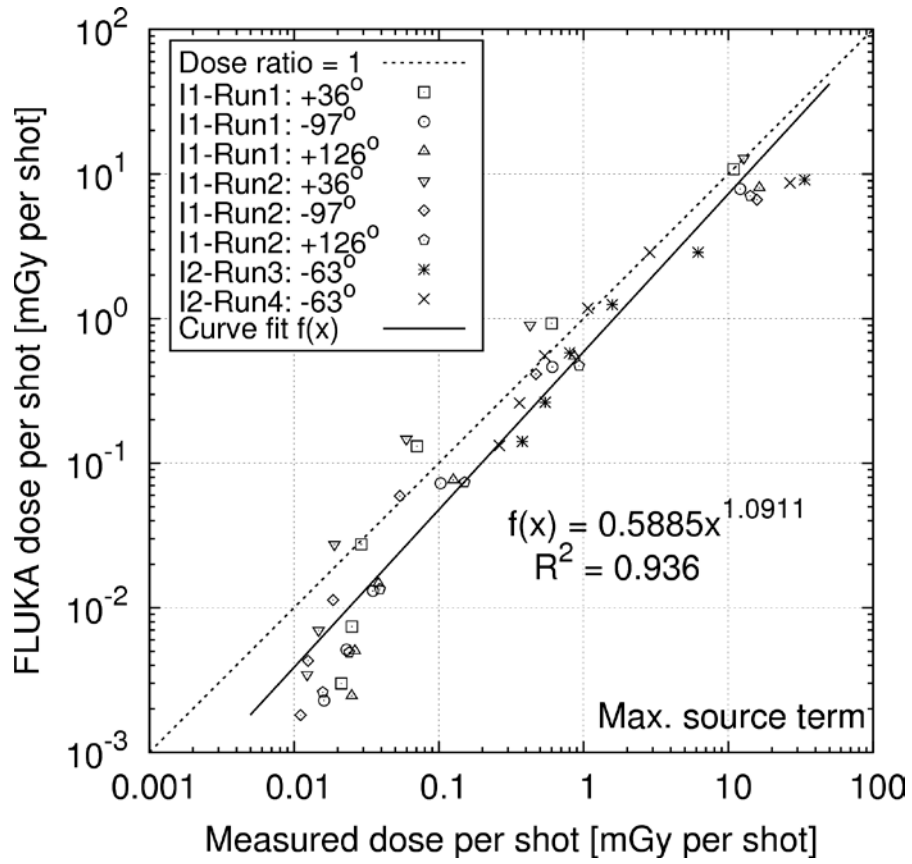


Fig. 8.

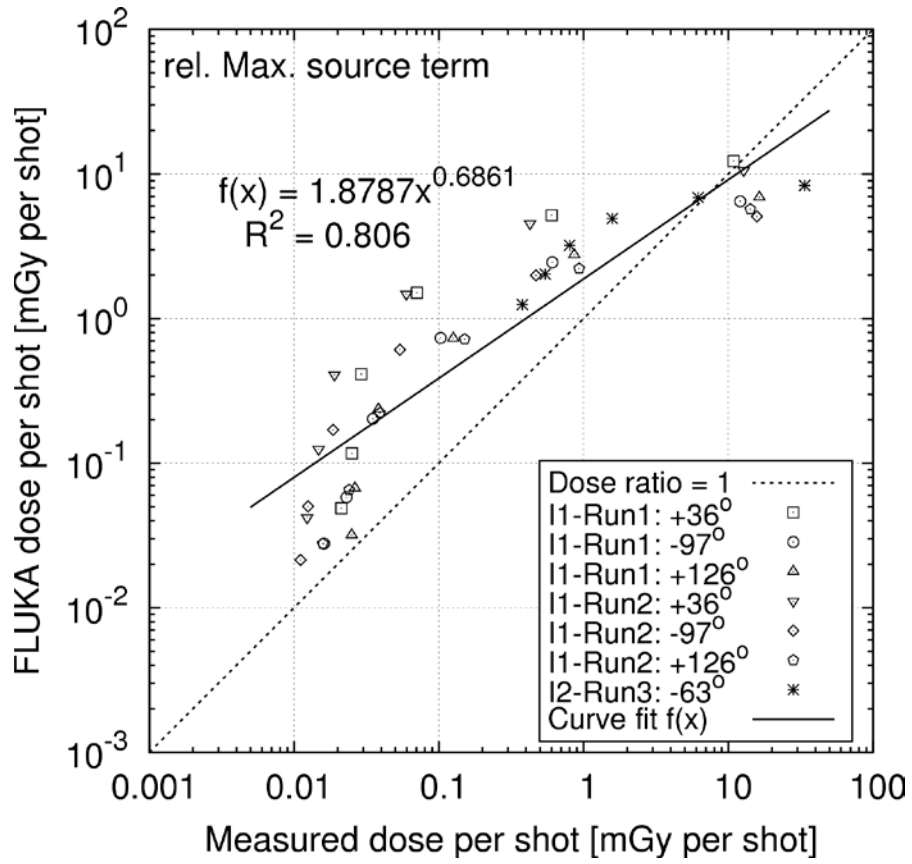


Fig. 9.

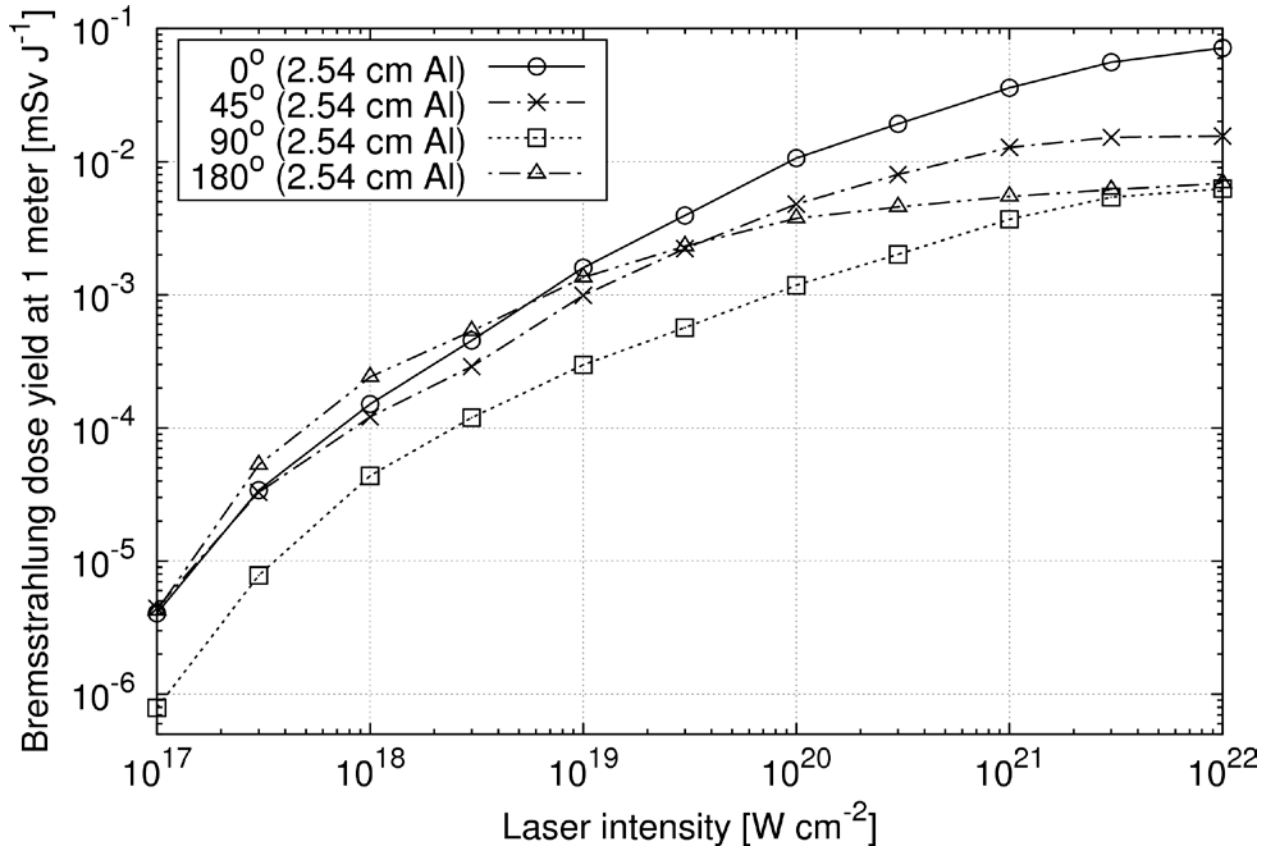


Fig. 10.

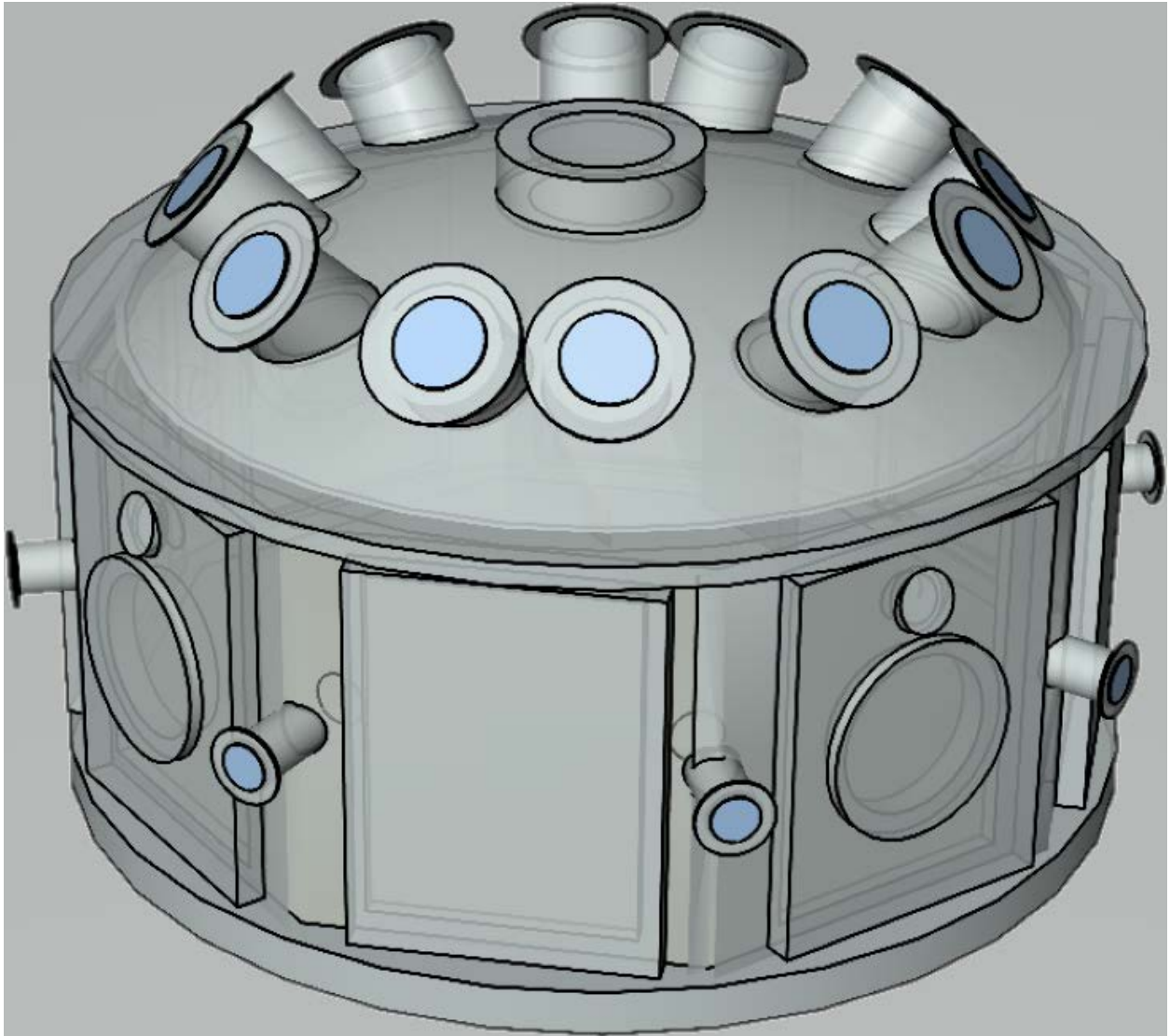


Fig. 11.

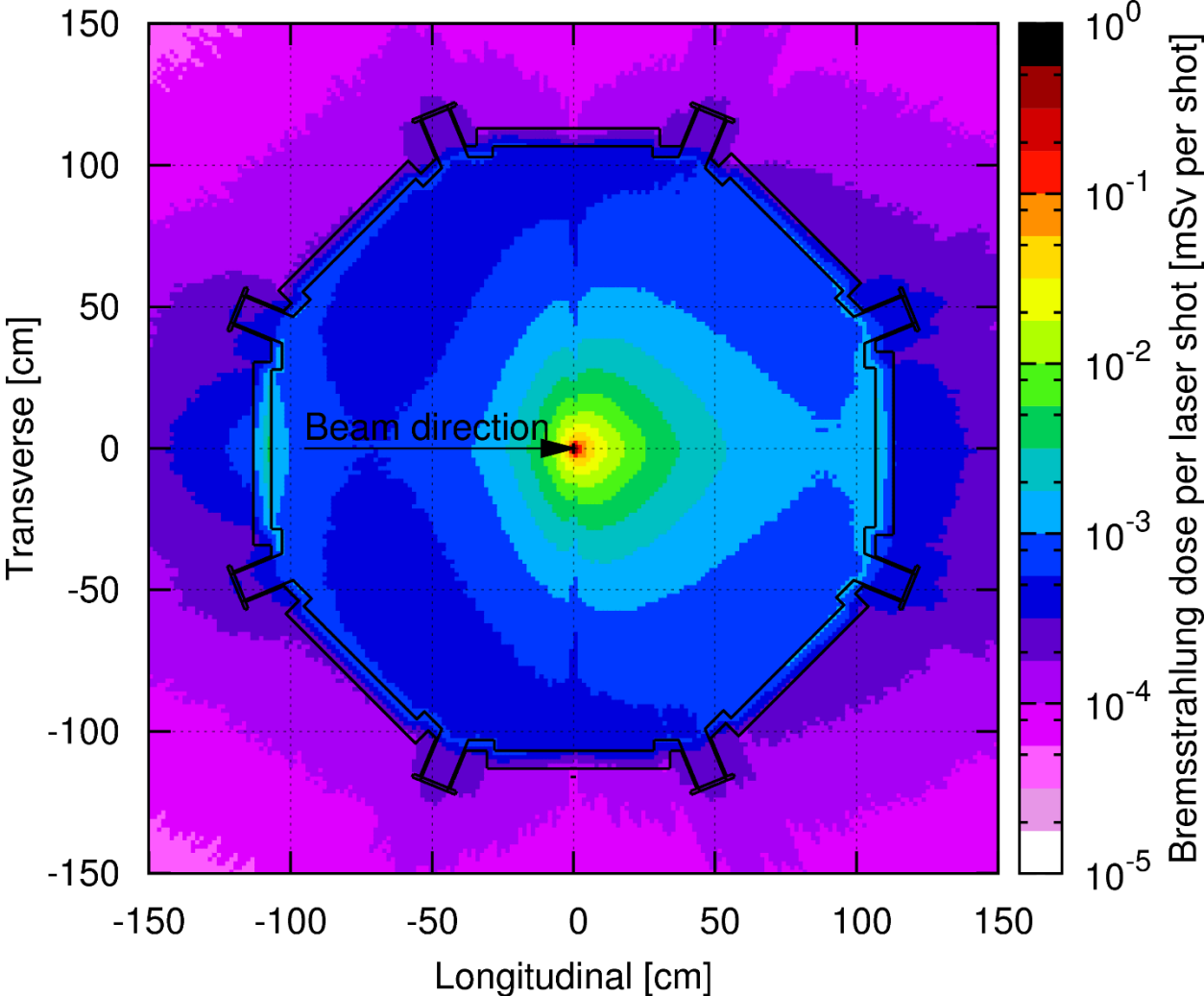


Fig. 12.

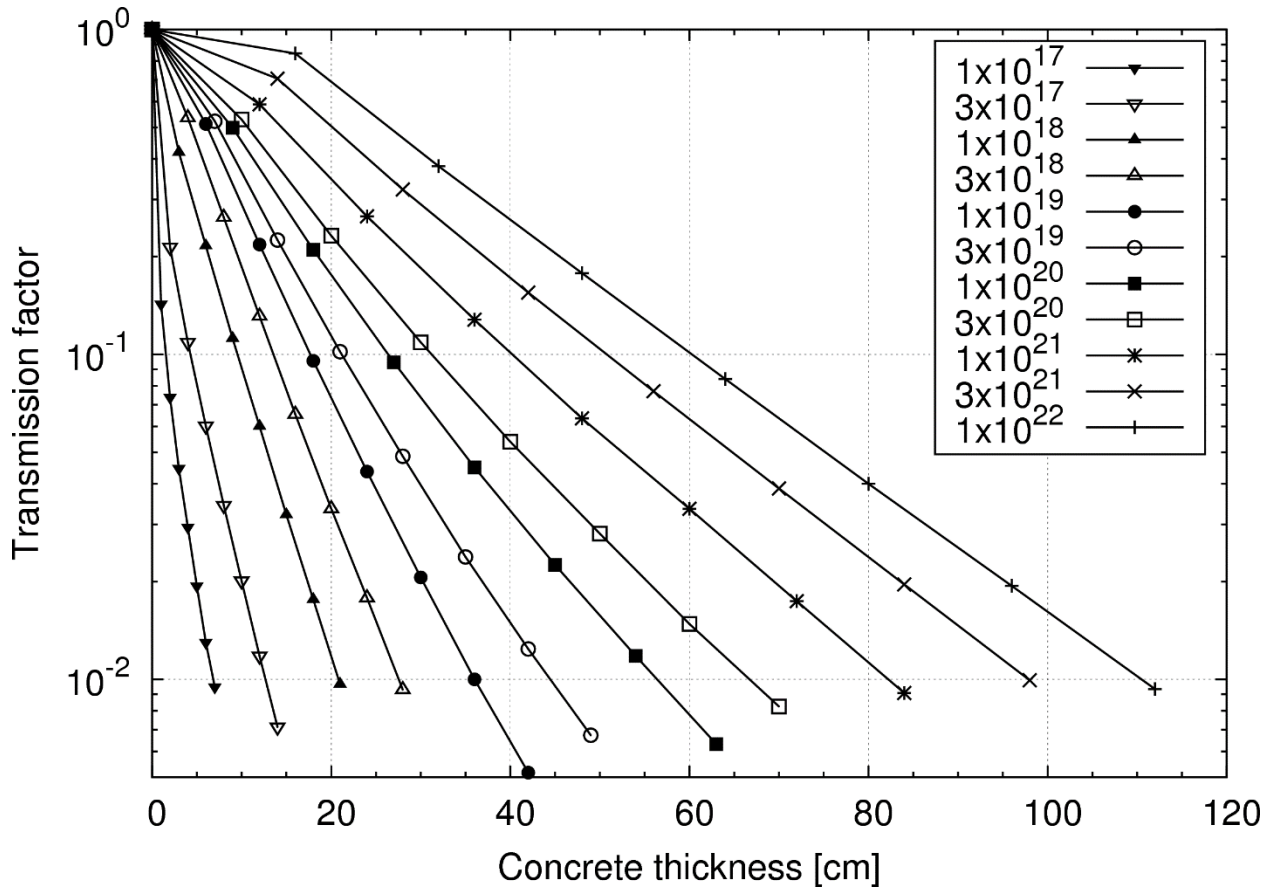


Fig. 13.

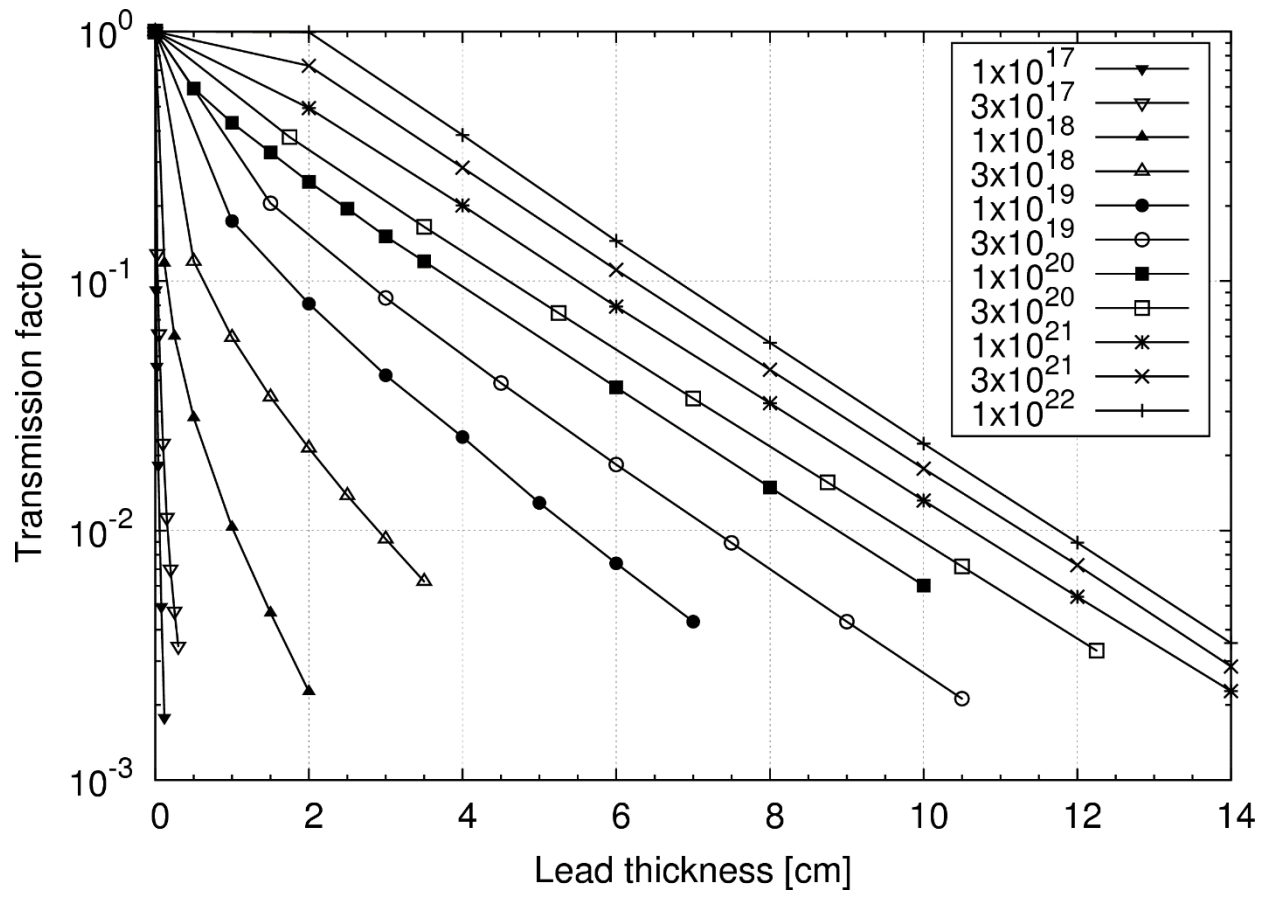


Fig. 14.

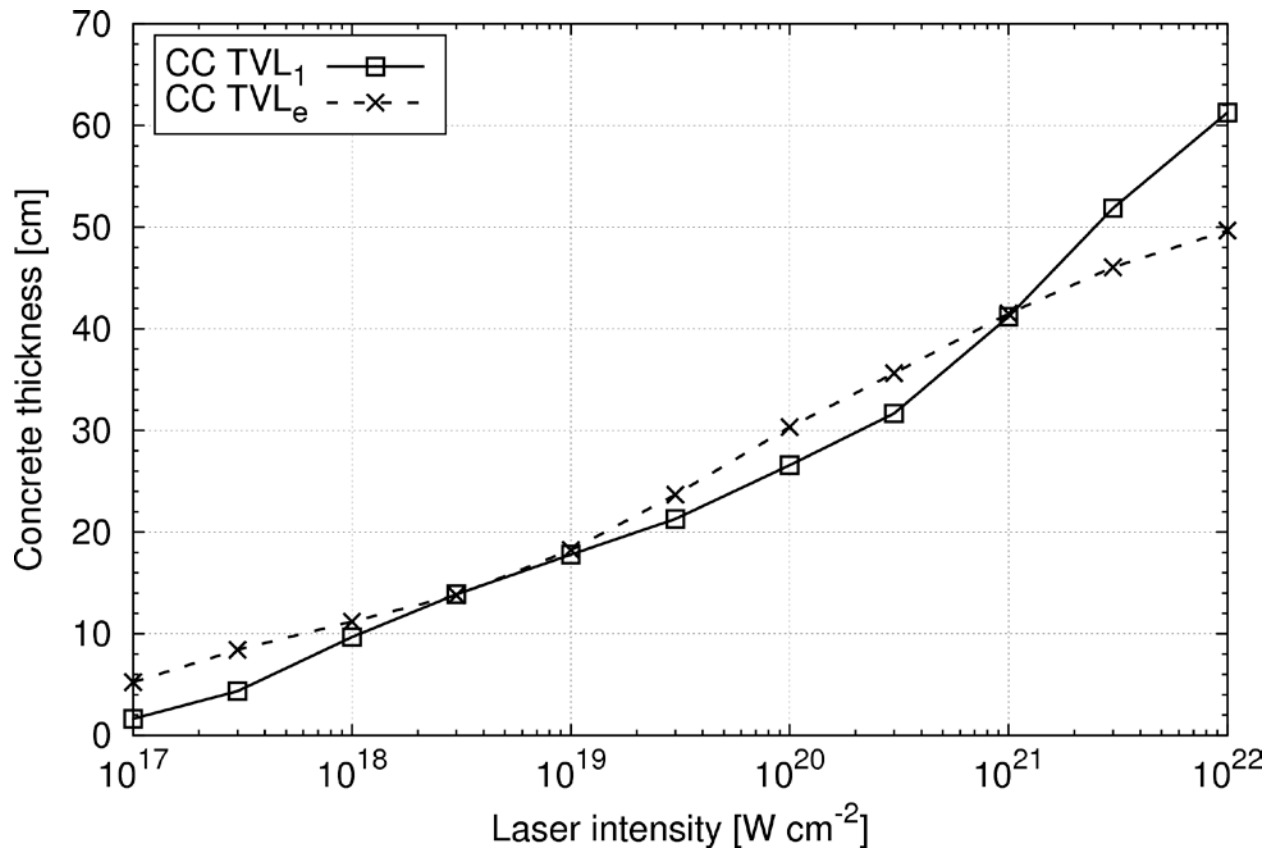


Fig. 15.

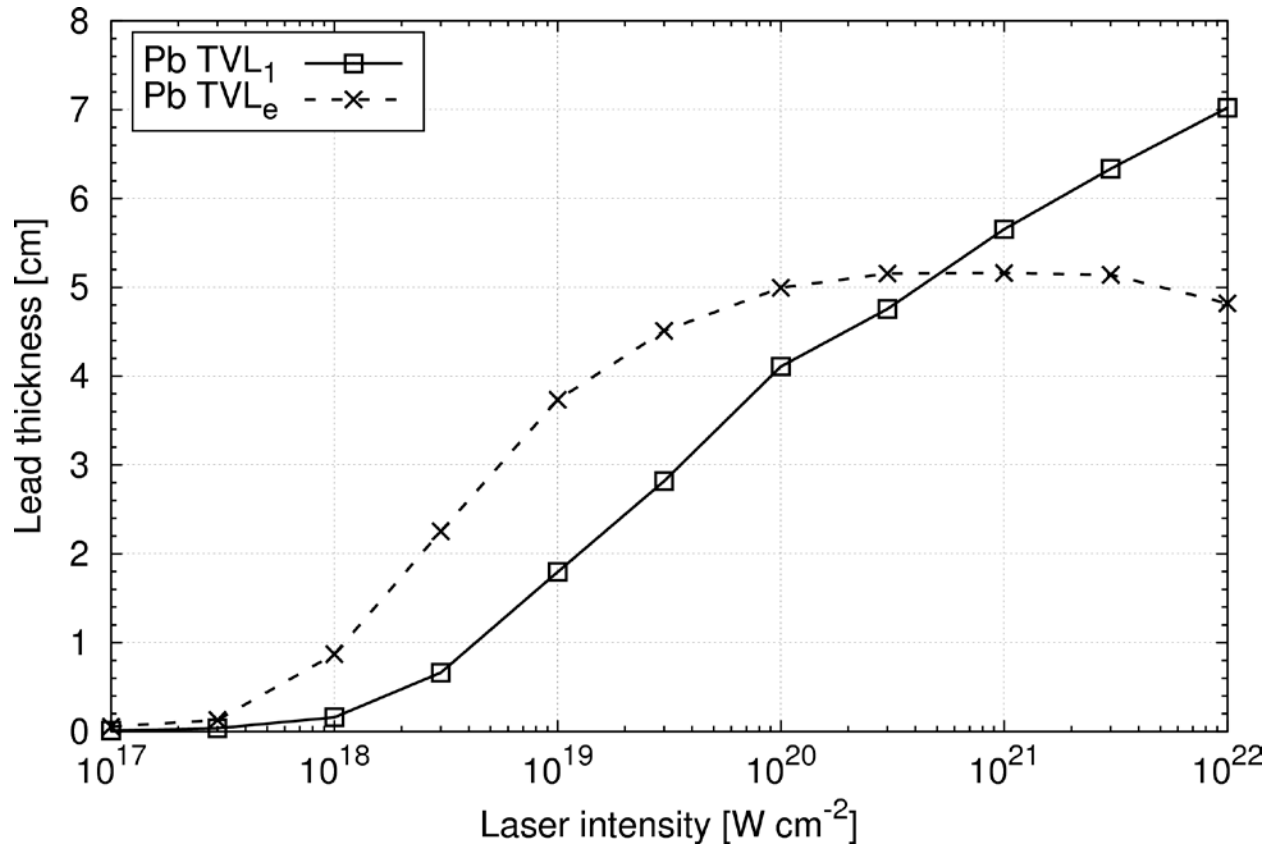


Fig. 16.

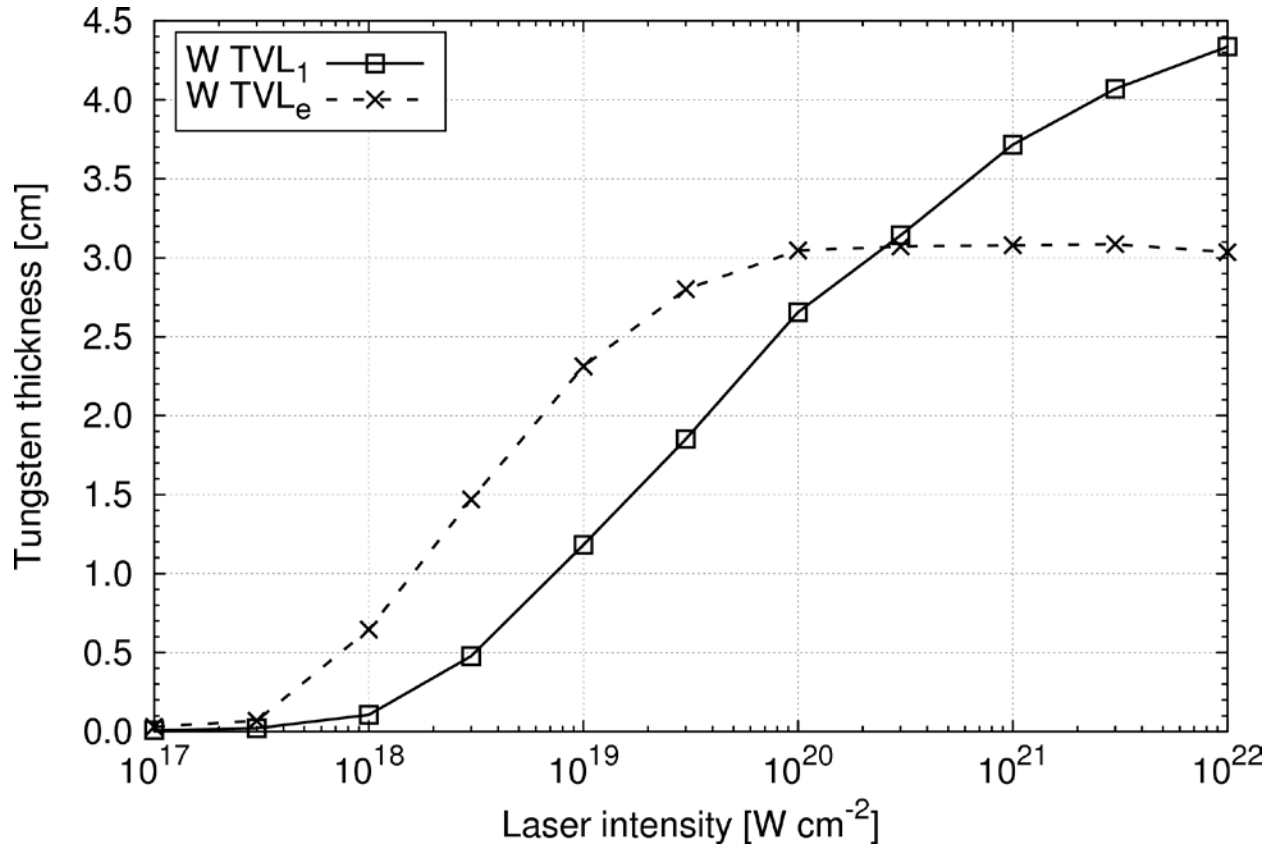


Fig. 17.

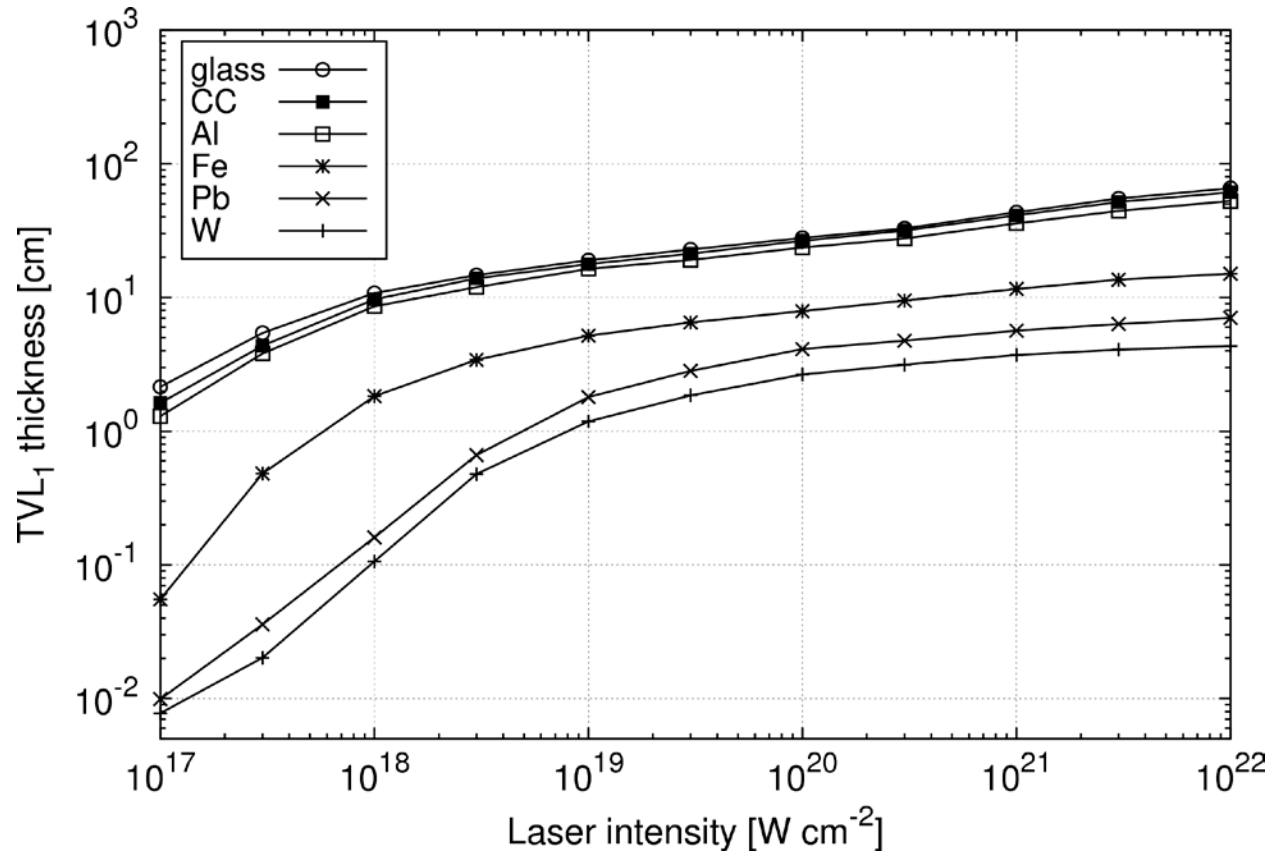


Fig. 18.

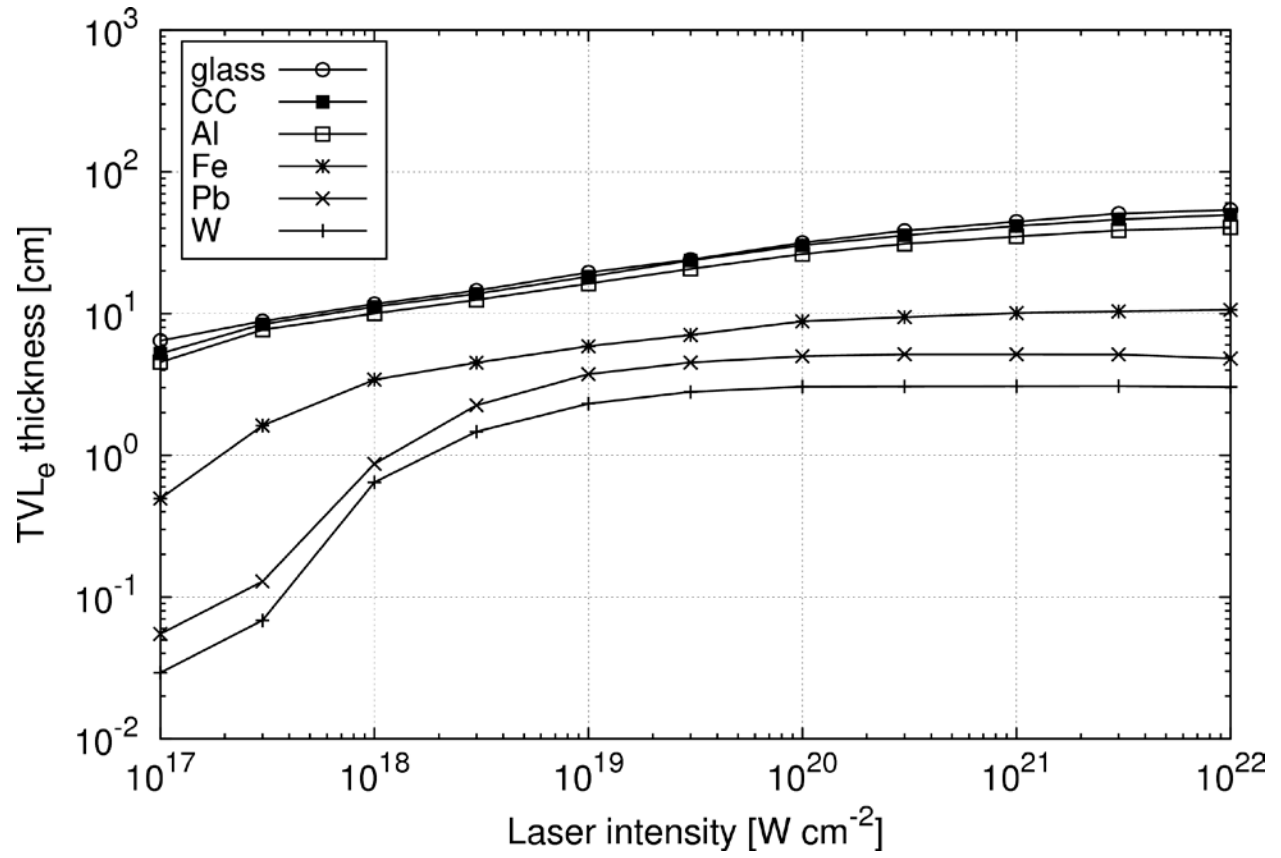


Fig. 19.